ELSEVIER

Journal of Atmospheric and Solar-Terrestrial Physics 70 (2008) 564–573

Journal of ATMOSPHERIC AND SOLAR-TERRESTRIAL PHYSICS

www.elsevier.com/locate/jastp

An effort to derive an empirically based, inner-magnetospheric electric field model: Merging Cluster EDI and EFW data

P.A. Puhl-Quinn[a,*], H. Matsui[a], V.K. Jordanova[b], Y. Khotyaintsev[c], P.-A. Lindqvist[d]

[a]*Space Science Center, University of New Hamsphire, Durham, NH 03824, USA*
[b]*Los Alamos National Laboratory, Los Alamos, NM 87545, USA*
[c]*Swedish Institute of Space Physics, SE-751 21 Uppsala, Sweden*
[d]*Royal Institute of Technology, SE-100 44 Stockholm, Sweden*

Accepted 27 August 2007
Available online 5 October 2007

Abstract

A key ingredient for modelling many inner-magnetospheric processes is the realistic representation of the spatio-temporal dynamics of the inner-magnetospheric electric field, or, IMEF. The Cluster Mission provides a unique opportunity to construct an IMEF model using electric field measurements from both the electron drift instrument (EDI) and the electric fields and waves instrument (EFW). A superset of IMEF data is formed by merging EDI and EFW data. Challenges presented by the merging process include the handling of compromised perpendicular electric field ($\mathbf{E}_{\perp}$) calculations, electric field offsets, scaling problems, and spurious fields. The present goal is to produce the highest quality merged IMEF data set possible which is minimally affected by these issues. Preliminary investigation of the merging process on Cluster 1 for the years 2001–2003 has revealed that merging is a worthwhile exercise. The data sets are shown to be complementary, and the IMEF merged data set is superior to either data set alone in terms of improved spatial coverage, and coverage of a wider range of geomagnetic activity levels. Preliminary use of the merged IMEF data set to construct a parameterized, equatorial, electric field model for the inner magnetosphere, the UNH-IMEF model, is also presented. The electric field morphology produced by this preliminary version of the UNH-IMEF model shows the expected sensitivity to IMF orientation.

PACS: 94.30.cb; 94.20.Ss; 94.30.cs; 94.80.+g

Keywords: Inner magnetosphere; Electric fields; Current system; Plasma convection; Instrumentation for space plasma physics; Magnetosphere

1. Introduction

The inner-magnetospheric electric field (IMEF) strongly controls the morphology and dynamics of the ring-current (e.g., Wygant et al., 1998; Jordanova et al., 2003, 2006) and plasmasphere

*Corresponding author. Tel.: +1 603 8623695; fax: +1 603 8620311.
E-mail address: pamela.puhlquinn@unh.edu (P.A. Puhl-Quinn).

1364-6826/$ - see front matter © 2007 Elsevier Ltd. All rights reserved.
doi:10.1016/j.jastp.2007.08.069

(e.g., Carpenter et al., 1993; Goldstein et al., 2003; Darrouzet et al., 2004; Liemohn et al., 2004). The IMEF formation and dynamics in turn are controlled by magnetospheric coupling to both the solar wind and the ionosphere. One of the simplest representations of the IMEF is the superposition of a constant, global, cross-tail merging electric field (due to solar wind driving), and the corotation electric field. Complicating this simple picture are the time-dependent nature of the driving field due to its dependence on solar wind velocity and the interplanetary magnetic field (IMF), the fact that the inner magnetosphere acts to "shield" itself from this driving field (e.g., Vasyliunas, 1970) and also responds sensitively to abrupt changes in the driving field (leading to "overshielding" and "undershielding" situations which can be associated with penetration electric fields, e.g., Huang et al., 2006), and that other meso-scale electric field structures associated with the formation of an asymmetric ring current (in particular, sub-auroral polarization streams (SAPS) and related sub-auroral ion drift (SAID), e.g., Galperin et al., 1974; Spiro et al., 1979; Foster and Burke, 2002; Goldstein et al., 2005; Puhl-Quinn et al., 2007) are set up during geomagnetically active periods. Ultimately, the most accurate IMEF description must produce the requisite charged particle dynamics of the inner magnetosphere which can occur over a broad range of temporal and spatial scales. These issues are addressed in much greater depth by the IMEF numerical experiments of Garner (2003), and Liemohn et al. (2006).

The IMEF description has been undertaken by several studies. They include both magnetospheric and "mapped" ionospheric representations. By "mapped", we mean the mapping of ionospheric electric potential patterns to the SM equatorial plane assuming equipotential field lines, and using a parameterized magnetic field model, such as that of Tsyganenko (2002). Magnetospheric representations include those of Volland (1973) and Stern (1975) (V–S) and the E5D model of McIlwain (1986). Ionospheric representations include the assimilative mapping of ionospheric electrodynamics (AMIE) model (Richmond and Kamide, 1988) and the ionospheric potential models of Weimer (1996, 2001) (hereafter referred to as W96 and W01, respectively). There are, of course, several other published electric potential/field descriptions (e.g., Baumjohann and Haerendel, 1985; Papitashvili et al., 1994; Papitashvili and Rich, 2002; Haaland et al., 2007). We focus, however, on V–S, E5D and W96/01 because of their relatively wide use and recent assessment in the inner magnetosphere.

The V–S model is a semi-empirical, analytic expression for the global, scalar electric potential of the Earth's inner magnetosphere. The electric field is constructed as the superposition of a "shielded" cross-tail electric field (convection) with a corotation electric field. The V–S electric convection potential was originally written as a function of the cross-polar cap potential. Subsequent parameterization by the *Kp* index was derived by Maynard and Chen (1975) using Ogo 3 and 5 midnight plasmapause observations. An optimal shielding parameter of ≈ 2 was empirically found by several studies (for a more recent discussion, see Korth et al., 1999). The E5D model is an analytic representation of the magnetospheric electric field which was constructed using particle measurements on the ATS-5 satellite at geosynchronous orbit. It is also geomagnetic activity level dependent, and has a shielding function. The *Kp*-dependence of the E5D model originally prescribed was found to be unrealistic and subsequently modified by Liemohn et al. (2001). The AMIE procedure is the synthesis of data from several different sources (including magnetic perturbations at ground and satellite heights, electric fields from radars and satellites and electric currents from radars) in order to produce ionospheric electric potential patterns. The mapping of AMIE convection electric potentials (MACEP) to generate inner-magnetospheric equatorial convection potentials, as well as the inclusion within the AMIE/MACEP framework of an asymmetric ring current driven penetration electric field (Ridley and Liemohn, 2002) was developed by Boonsiriseth et al. (2001). The W96/W01 models are empirical, high-latitude, ionospheric electric potential models constructed using Dynamics Explorer-2 satellite vector electric field instrument (VEFI) data. W96 is parameterized by IMF, solar wind velocity, and dipole tilt angle. W01 is an improved version of W96 in which a substorm component is added by allowing optional parameterization by the *AL* index.

Several metrics have been designed to assess an IMEF model's ability to realistically control charged particle dynamics of inner-magnetospheric systems. Models describing inner-magnetospheric particle transport and energization are often developed such that an arbitrary IMEF description can be used as

a driver. The strengths and weaknesses of various IMEF models can then be assessed. The IMEF models described above have received mixed reviews. For example, Jordanova et al. (2003) used both V–S and MACEP to drive the ring current–atmosphere interaction model (RAM) to study storm-time ring current evolution. They found that the MACEP model outperformed the V–S model, especially during the storm's main phase, because of its higher spatial and temporal resolution. Liemohn et al. (2004) used modified E5D, mapped W96 and a self-consistent IMEF description to drive a version of RAM coupled to the dynamic global core plasma model (DGCPM) to study plasmapause shape during the storm-time recovery phase. They found the self-consistent model to be the best choice, followed by W96 and then E5D. Friedel et al. (2001) and Korth et al. (1999) both used activity-dependent V–S to derive theoretical ion and electron Alfvén boundary layer locations and compare them to statistical locations derived from in situ satellite data. They found that in terms of average, global transport, over a wide range of geomagnetic activity, the V–S model did exceptionally well. And finally, Angelopoulos et al. (2002) examined the sensitivity of storm-time ion phase space modelling to the IMEF description by using V–S, W96, W01 and event-specific, modified Weimer models. They found that none of the models could alleviate significant model/data differences, and proposed that inductive electric fields and/or nighside injections are likely to improve the situation.

This study is unique in that it introduces the development of an empirically based, parameterized IMEF model, hereafter referred to as the UNH-IMEF model, using near-equatorial electric field measurements in the $4<L<10$ range from the Cluster data set which spans 2001-present. Past efforts to characterize the dynamics of the IMEF from in situ data reveal important information, but generally have a smaller scope. Electric field measured by ISEE 1 is limited inside the plasmasphere (Maynard et al., 1983). Electric field measurement by CRRES consists of 14 months (Rowland and Wygant, 1998). Their statistical electric field pattern has limited coverage in magnetic local time, although reliable electric fields are obtained outside the plasmasphere.

Preliminary groundwork for the UNH-IMEF model is found in the work of Matsui et al. (2003, 2004). In these initial investigations, data from the Cluster electron drift instrument (EDI) (Paschmann et al., 2001) were used to construct inner-magnetospheric potential maps. As EDI measures the drift step of artificially emitted electrons whose gyroradii are much larger than the size of the spacecraft, the electric field calculated is not affected by photoelectrons around the spacecraft. However, as discussed in the following section, the electron beams do not always come back to the detectors, causing data gaps. In this study, we have included electric field data from the Cluster electric fields and waves (EFW) experiment (Gustafsson et al., 2001) in order to compensate for these gaps. The purpose of this paper is to report on a preliminary IMEF data merging study using Cluster 1 EDI and EFW data from 2001–2003, and also report on a preliminary version of the UNH-IMEF model which uses this merged data set.

2. Merging EDI and EFW data

There are two instruments for measuring the electric field on Cluster: EDI and EFW. As mentioned above, EDI utilizes the electron gun technique with electron beam energies of either 1 or 0.5 keV. EDI's primary measurement is the drift velocity of these electrons. The convection electric field, or, $\mathbf{E}_\perp$ is then derived using drift velocity and the magnetic field measurements. The EDI data we use is the 4-s resolution prime parameters. The other instrument, EFW, operates two pairs of double probes in the spin-plane. EFW's primary measurement is the electric field in the spin-plane of the spacecraft. The spin-axis component is estimated by assuming $\mathbf{E}\cdot\mathbf{B}=0$. We use the EFW L3 data product found at the Cluster Active Archive (Lindqvist et al., 2006), which also has a 4-s cadence.

The merging of the EDI and EFW $\mathbf{E}_\perp$ data in the inner magnetosphere is a useful exercise because of the complementarity of the two data sets. As mentioned above, $\mathbf{E}_\perp$ is a derived parameter for each of the instruments. Gaps in the $\mathbf{E}_\perp$ data sets, therefore, can result from factors other than primary measurement failure. Table 1 lists reasons for either non-existent (Reasons 0–1) or compromised (Reasons 2–5) $\mathbf{E}_\perp$ data for each instrument. These issues are described in detail in Eriksson et al. (2006). We will briefly describe these issues in the context of the present inner-magnetospheric study.

Neither instrument operates 100% of the time in science mode. As for primary measurement failure, EDI is sensitive to large 0.5–1 keV background

Table 1
Reasons for either non-existent or compromised $\mathbf{E}_\perp$ data

EDI	EFW
(0) Non-science operating mode	(0) Non-science operating mode
(1) Measurement failure due to:	(1) Measurement failure
High keV e^- flux	(2) Sub-optimal analysis conditions
High **E** variance	(e.g., "alpha-angle" problem)
High **B** variance	(3) Photoemission asymmetry
(2) Sub-optimal analysis conditions	(4) Partial shielding
(e.g., poor triangulation result)	(5) Spurious fields

electron fluxes that can overwhelm the signal from its returning electron beam. In addition, electromagnetic field temporal variations with frequencies much higher than the spin frequency of the spacecraft can overwhelm the beam tracking mechanism (Quinn et al., 2001). Concerning spin resolution data (4-s cadence), this can result in data dropout (i.e., no measurements returned during an entire spin), or compromised $\mathbf{E}_\perp$ calculation because of either too few measurements within the spin and/or measurements with such great temporal variability that the assumption of electromagnetic field stability within the spin period is invalid. This is referred to in the table as "poor triangulation result". For EFW, the use of the $\mathbf{E}\cdot\mathbf{B}=0$ assumption leads to a major analysis hurdle when the magnetic field orientation lies close to the spin-plane. This is referred to as the "alpha-angle" problem. It leads to a compromised $\mathbf{E}_\perp$ calculation because the denominator (and also possibly the numerator) in the expression for the spin-axis component of the electric field goes to zero. We have tried to minimize the amount of compromised EDI and EFW $\mathbf{E}_\perp$ data by only using the highest quality triangulation results from EDI and by limiting the use of EFW data to those data where the magnetic field is oriented greater than 15° from the spin-plane.

Three other reasons for compromised EFW $\mathbf{E}_\perp$ data listed in Table 1 are those which do not affect EDI data. An asymmetric photoelectron cloud produces a close-to-constant sunward offset field. Partial shielding, or, the Fahleson effect, results from the effective antenna length being slightly shorter than the physical probe separation (Pedersen et al., 1984). And finally, spurious fields due to, for instance, electrostatic wakes created by supersonic ion flows in a tenuous plasma, contaminate the measurement of the ambient electric field (Eriksson et al., 2006; Engwall et al., 2006).

EDI and EFW $\mathbf{E}_\perp$ data are complementary so that a merged data set will have better coverage. It is often the case that when one experiment fails to produce a viable $\mathbf{E}_\perp$ calculation, the other experiment is successful. Fig. 1 illustrates three case studies that illustrate this point. The electric field component in the X-DSI (despun-satellite-inverted, which is approximately GSE) direction is shown for the perigee passes of 20011002, 20020418 and 20010704 (top to bottom). EDI data are plotted in black, while EFW is plotted in red. The shaded regions are where **B** is within 15° of the spin-plane. Therefore, no EFW data are shown for these shaded regions since it is excluded from the merging process.

The top panel illustrates that EDI compensates for EFW's "alpha-angle" problem on both sides of the magnetic equator, whereas EFW compensates for EDI's high keV e-flux problem near the magnetic equator. The middle panel, 20020418, shows that EDI data are almost completely absent during this pass because of high geomagnetic activity levels, while EFW is successful and showing strong variations. The *Dst*-index shows a medium storm commencing the previous day on 20020417 at 12:00UT; at the time of the Cluster observations, *Dst* averages −115 nT and is within a local minimum. The bottom panel shows how again, EDI compensates for the "alpha-angle" problem, and also shows how spurious fields near the magnetic equator contaminate the EFW measurement. The spurious fields are discussed later in this section. We focus now on the complementarity of the two data sets.

After examining the data from 2001 to 2003, it was found that one of the main strengths of the EDI data set in terms of complementarity is its insensitivity to the "alpha-angle" problem, as illustrated in Fig. 1. Statistically, Fig. 2 illustrates how often we have the "alpha-angle" problem at Cluster in the inner magnetosphere. Plotted is the percentage of time the "alpha-angle" problem is encountered in the inner magnetosphere as a function of magnetic latitude and magnetic local time sector. The data were compiled using Cluster 1 magnetic field and spin-axis orientation data that lies within 2 h of the crossing of the magnetic equator near perigee for the years 2001–2003. The data were then binned in 5° magnetic latitude bins, and 6-h MLT bins

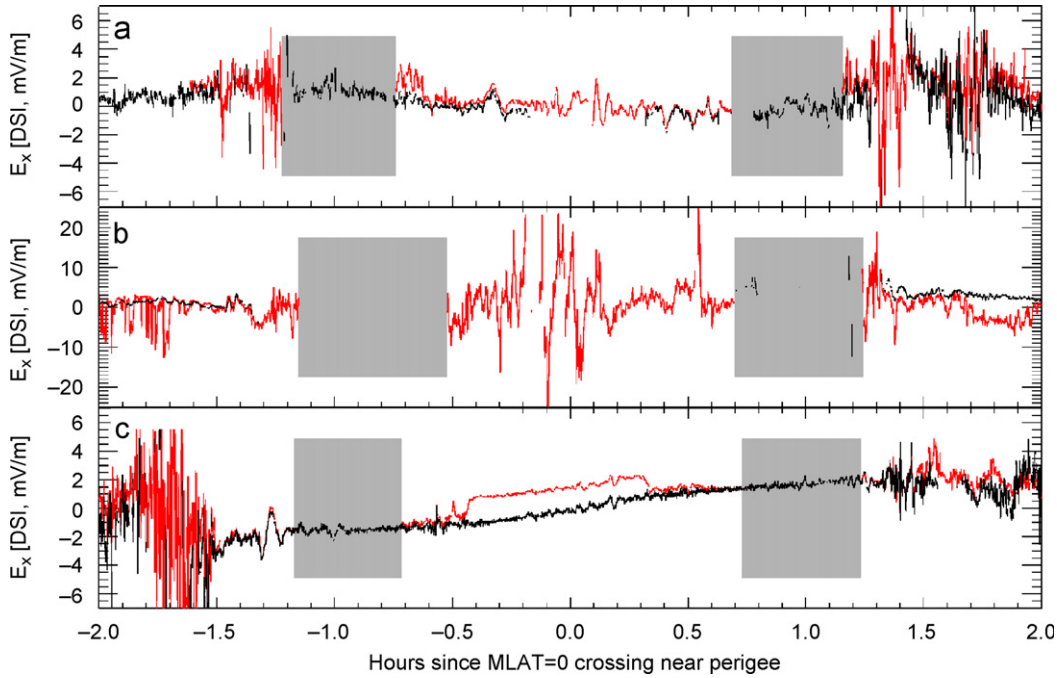

Fig. 1. Three case studies illustrating the complementarity of Cluster EDI (black) and EFW (red) data in the inner magnetosphere. The electric field component in the X-DSI (despun-satellite-inverted, which is approximately GSE) direction is shown for the perigee passes (a) 20011002, SC 1, MLAT=0 at 22:17:30 UT; (b) 20020418, SC 2, MLAT=0 at 08:50:30 UT; and (c) 20010704, SC 1, MLAT=0 at 11:33:30 UT. The data are plotted as a function of time in units of "hours since the crossing of the magnetic equator." The shaded regions are where **B** is within 15° of the spin-plane.

centered on midnight (blue), dawn (red), noon (orange) and dusk (green). This figure shows that the "alpha-angle" problem occurrence rate peaks at magnetic latitudes in the range of ≈ -35 to -25 ($+35$ to $+40$) degrees in the southern (northern) hemisphere for all MLT sectors, and that the peak occurence values approach 90%. Although the EDI performance during all "alpha-angle" affected periods is not presented, it is assumed that EDI's contribution to a merged data set for these periods would be significant since the EFW $\mathbf{E}_\perp$ data are compromised during these times.

The EFW data set is quite complementary to the EDI data set since it has better 5-min averaged data statistics at larger levels of geomagnetic activity than EDI. (Note: 5-min averages are used in the construction of the UNH-IMEF model.) Fig. 1b illustrated this point, as described above. Fig. 3 shows statistically the amount of $\mathbf{E}_\perp$ data in the inner magnetosphere for Cluster EDI and EFW as a function of *Kp*, which is an indicator of geomagnetic activity level. The top panel shows the number of 5-min averaged data points as a function of *Kp* for EDI (dashed) and EFW (solid) data. The bottom panel shows the number of 4-sec data points comprising each 5-min averaged data point as a function of *Kp* for EDI (dashed) and EFW (solid). If there are no data gaps in the 4-s data, each 5-min averaged point would be constructed from 75 4-s data points. This figure illustrates that while EDI and EFW have the same number of 5-min averaged data points (top panel), the number of 4-s data comprising those averages is much less for EDI at larger values of *Kp* (bottom panel). Therefore, we can assume that for larger *Kp* values, the 5-min cadence merged data are more statistically robust.

A by-product of the merging process is the comparison study of temporally simultaneous EDI and EFW $\mathbf{E}_\perp$ data. This is quite useful for the study of offsets, scaling and spurious fields. A study of constant offset and scaling has not been completed at this time. Regarding spurious fields, EDI and EFW data have been compared previously to diagnose spurious fields found in the polar cap (Eriksson et al., 2006) and magnetotail lobe (Engwall et al., 2006) regions. Our investigation concerns spurious fields found in the inner magnetosphere, like those shown in Fig. 1c). Significant

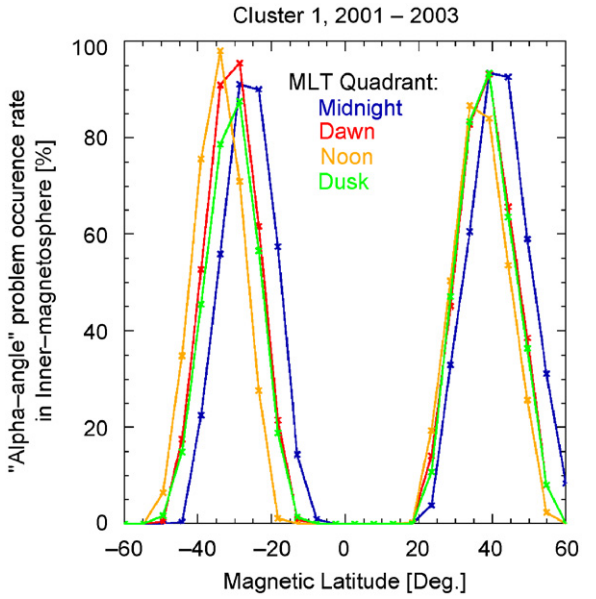

Fig. 2. Diagnosing the "alpha-angle" problem in the inner magnetosphere. Plotted is the percentage of time the "alpha-angle" problem is encountered in the inner magnetosphere as a function of magnetic latitude and magnetic local time sector. The data were compiled using actual Cluster 1 magnetic field and spin-axis orientation data that lies within 2 h of the crossing of the magnetic equator near perigee for the years 2001–2003. The data were binned in 5° magnetic latitude bins, and 6-h MLT bins centered on midnight (blue), dawn (red), noon (orange) and dusk (green).

differences in the electric fields ($\geqslant 2\,\mathrm{mV/m}$) measured by EFW and EDI have been found for several perigee passes, when the spacecraft potential was getting close to zero ($\leqslant 0.8\,\mathrm{V}$). Preliminary investigation shows that the error resides in the EFW measurements and the spurious field can be reconstructed using the EDI and magnetic field data. Modeling shows that the spurious field has a general dependence on the spacecraft potential and has the following major components: (1) Sun directed, (2) magnetic field aligned, (3) spacecraft velocity aligned, and (4) plasma convection aligned. (1) and (2) are related to the photoelectron cloud asymmetry, while (3) and (4) are related to wakes created by fast spacecraft motion and/or plasma convection. Further work is necessary to estimate the relative importance of these components and to estimate the feasibility for automatic detection and correction of such errors in the EFW data.

A simple merging algorithm has been applied to Cluster 1 EDI and EFW data for the years 2001–2003. EDI data are favored over EFW data at those times when both return an $\mathbf{E}_\perp$ calculation.

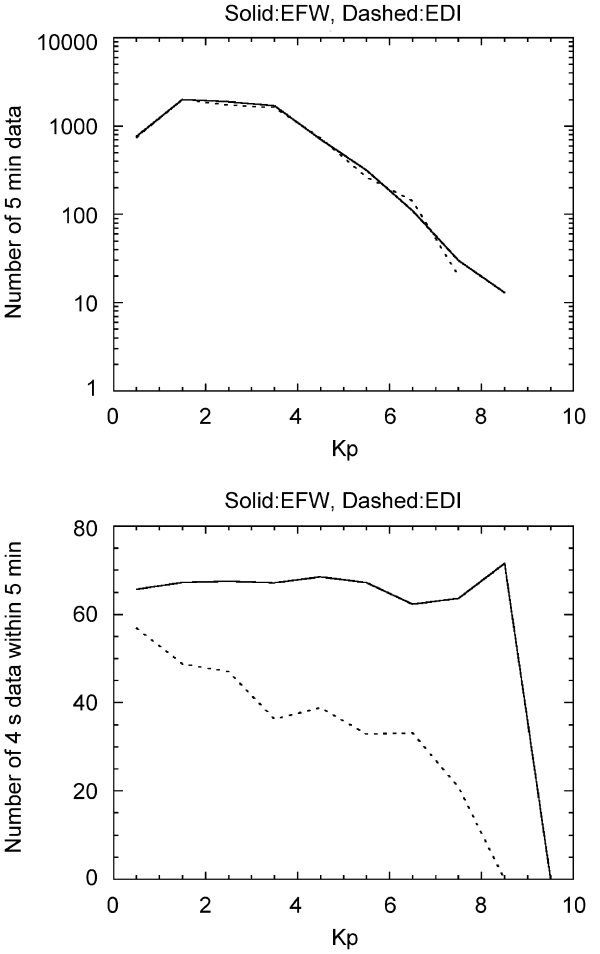

Fig. 3. The *Kp* dependence of the amount of $\mathbf{E}_\perp$ data in the inner magnetosphere for Cluster EDI and EFW. The top panel shows the number of 5-min averaged data points as a function of *Kp* for EDI (dashed) and EFW (solid) data. The bottom panel shows the number of 4-s data points comprising each 5-min averaged data point as a function of *Kp* for EDI (dashed) and EFW (solid). If there are no data gaps in the 4-s data, each 5-min averaged point would be constructed from seventy five 4-s data points.

Care has been taken to account for spurious fields in the EFW data set, especially when no EDI data are available. Fig. 4 illustrates the improvement in data coverage achieved through merging the EDI and EFW data sets in the inner magnetosphere as a function of MLT. Notice that the MLT of perigee corresponds to a particular month, denoted underneath the MLT values. Again, the inner-magnetospheric data are defined to be that data which is within ± 2 h of the magnetic equator crossing near perigee. This figure shows that inner-magnetospheric (IM) data coverage is improved by an overall factor of ≈ 2.

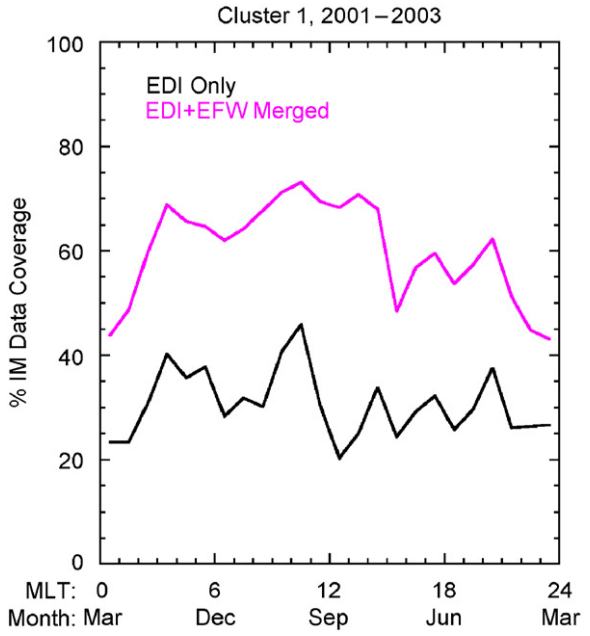

Fig. 4. Improved data coverage achieved through merging the EDI and EFW data sets in the inner magnetosphere (IM) as a function of MLT. The MLT of perigee corresponds to a particular month, denoted underneath the MLT values. Data coverage using only EDI data is plotted in black, and the coverage using the merged data (EDI + EFW) is plotted in magenta. The IM data are defined to be that which is within ±2 h of the magnetic equator crossing near perigee.

3. Global convection patterns using the merged data set

The merged IMEF data set is used to construct a preliminary version of the UNH-IMEF model. This section shows how the UNH-IMEF average electric field patterns are organized by the polarity of the Z-component of the interplanetary magnetic field (IMF B_z). This is a natural choice for an initial parameterization study due to the well-established link between southward IMF (i.e., $B_z<0$) and increased geomagnetic activity level (e.g., Burton et al., 1975; Gonzalez et al., 1994). The same type of statistics were performed using only EDI data by Matsui et al. (2003). The average electric fields are calculated between $L=4$ and 10 in all MLT ranges after mapping to the equatorial plane in SM coordinates by using the Tsyganenko model (Tsyganenko, 2002). The interplanetary parameters with a proper propagation delay are taken from ACE (Smith et al., 1998; McComas et al., 1998).

The calculated patterns using Cluster 1 merged EDI/EFW IMEF data, from 2001 to 2003, are shown in the frame corotating with the Earth in Fig. 5. Plotted are convection direction vectors whose length corresponds to the magnitude of the electric field. From left to right are patterns calculated for IMF $B_z>0$, $-5<B_z<0$, and $B_z<-5$ nT, which we will refer to as P1, P2 and P3, respectively. The total amount of Cluster 1 merged IMEF data in this time period is ≈ 495 h worth (i.e., 445,500 4-s resolution data points). The amount of data comprising patterns (P1, P2, P3) are (275, 195, 25) h. The IMF B_z average values and standard deviations for (P1,P2,P3) are $(2.5\pm2.8, -1.8\pm-1.3, -7.5\pm2.7)$ nT. The amount of time the *Dst*-index is less than -100 nT for (P1, P2, P3) is (0, 0.75, 5) h. The global estimates for electric field standard deviation for (P1, P2, P3) are (0.8, 1.0, 1.0) mV/m. Two contributing factors for these estimates are measurement errors and natural waves such as ULF waves. The measurement errors are considered random errors and can be eliminated by the increasing number of data (Matsui et al., 2004). Natural waves have often large amplitudes and are known to be comparable to the average electric fields (Matsui et al., 2003). This is reserved for further studies.

The P1 and P2 patterns have basically the same characteristics as those previously calculated using EDI data alone: stronger convection, especially on the dusk-side, occurs for a more southward IMF orientation, indicating that the merging potential from interplanetary space depends on the polarity of IMF B_z. Nevertheless, these new patterns are statistically more robust because of the aforementioned improved coverage of the new merged data set. There is also a large asymmetry of the magnitude between dawnside and duskside, possibly caused by the asymmetry of the ionospheric conductivity (Wolf, 1970). The convection strength is even larger for P3, as expected, although spatial coverage has become an issue due to fewer data points for this IMF B_z range. For P3, the coverage tends to be worse around ~3 and ~15 MLT, possibly due to the Russell–McPherron (RM) effect (e.g., Kamide et al., 1998). For the Cluster perigee data set, these values of MLT correspond roughly to winter and summer, whereas the RM effect predicts higher geomagnetic activity levels in spring and fall. We cannot make a definite statement at this time as to what extent the RM effect is present in the Cluster IMEF data set, since the patterns constructed to-date use data from only one spacecraft, and span only 3 years. This will be, however,

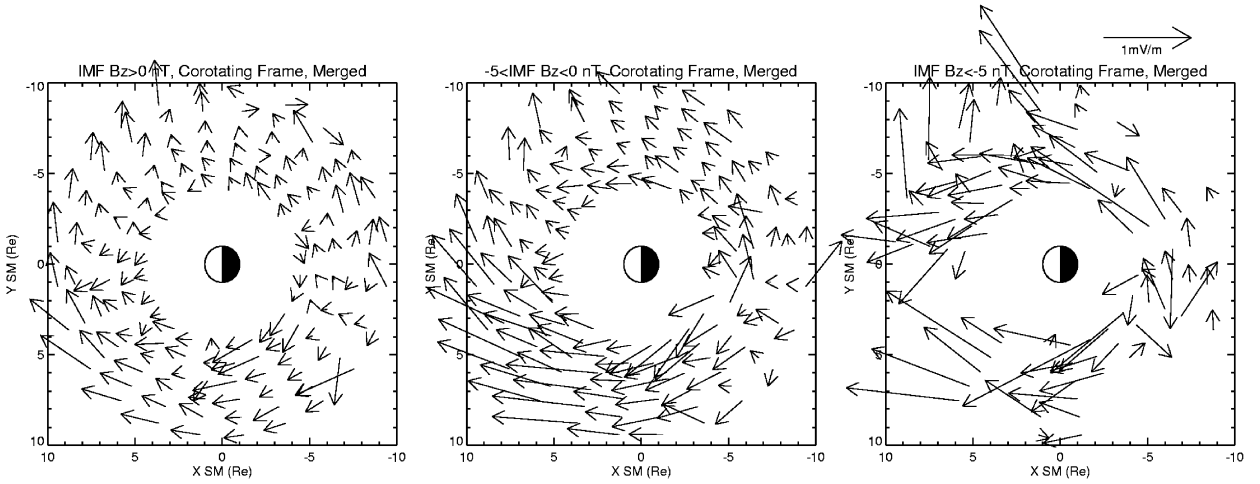

Fig. 5. Electric field magnitude and convection direction in the $X-Y$ plane. The length of the vector corresponds to the magnitude of the electric field. The scaling is denoted in the upper right-hand corner. The direction of the plotted vector is that of convection, so that the direction of the electric field is obtained by rotating 90°. in a counterclockwise direction. Merged EDI/EFW IMEF data from Cluster 1 from 2001–2003 were used to construct these patterns. The data have been sorted by the IMF orientation. From left to right are patterns calculated for IMF $B_z>0$, $-5<B_z<0$, and $B_z<-5$ nT.

a future topic of study as we refine and extend the merged data set.

A parameterization by solar wind speed, V_{sw}, was also performed (not shown). The data were sorted according to $V_{sw}<480$ and $V_{sw}>480$ km/s (patterns P1v and P2v, respectively). The convection differences between P1v and P2v were similar to those found between P1 and P2. This could be reflecting the fact that V_{sw} magnitude is known to correlate with southward IMF B_z strength within magnetic clouds (e.g., Gonzalez et al., 1998). It could also be a simple reflection of the interplanetary electric field's dependence on V_{sw}.

4. Summary

Knowledge of the spatio-temporal dynamics of the IMEF is key to the modelling of many inner-magnetospheric processes. Construction of a parameterized IMEF model from Cluster EDI and EFW data, the UNH-IMEF model, is being undertaken. The first step has been to merge EDI and EFW $\mathbf{E}_\perp$ data to create a superset. The $\mathbf{E}_\perp$ data superset is superior to either data set alone, because the EDI and EFW data are complementary. Compromised and/or non-existent $\mathbf{E}_\perp$ data are features of both data sets. It was shown that it is often the case that failure to produce viable $\mathbf{E}_\perp$ data on one instrument is often compensated for by the other instrument. One of the major strengths of EDI in terms of complementarity is its insensitivity to the "alpha-angle" problem, whereas EFW is more successful during periods of high geomagnetic activity levels. For Cluster 1 data from 2001 to 2003, it is shown that spatial data coverage improved by a factor of 2 after merging. Coverage in terms of geomagnetic activity levels also improved given the fact that EFW is better able to measure the turbulent fields found during storms and substorms. A byproduct of the merging process is the study of spurious fields at perigee when EDI and EFW have temporally simultaneous measurements. These spurious fields, which occur often, can exceed 2 mV/m and appear to be a function of spacecraft potential, and possibly caused by a combination of photoemission asymmetry and wakes. Their study is an ongoing investigation. Ultimately, a merged IMEF data set using Clusters 1, 2, 3 and 4 data, from the years 2001 present will be constructed that is minimally affected by compromised $\mathbf{E}_\perp$ data, offsets, scaling problems and spurious fields. This superset will be used in the construction of the UNH-IMEF model. The UNH-IMEF model will be an improvement over previous work done using only EDI data (Matsui et al., 2003, 2004) because of better spatial data coverage and an increased coverage of a wider range of geomagnetic activity levels. A preliminary version of the UNH-IMEF model shows the expected electric field morphology's sensitivity to IMF orientation and solar wind speed. The UNH-IMEF model will ultimately undergo further development (as the

merged IMEF data set is improved and augmented), and be used in a future study to drive the RAM ring current simulation.

Acknowledgments

We thank J. Quinn, R. Torbert and A. Eriksson for useful discussions. Work by P. Puhl-Quinn and H. Matsui has been supported by NASA Grants NAG5-9960, NNG04GA46G and NNG05GG50G. Work at Los Alamos was conducted under the auspices of the U.S. Department of Energy, with partial support from the NASA Living With a Star TR&T program. The Cluster Prime Parameter Data set was obtained through the Cluster Science Data System (CSDS) (http://cl1.plasma.mpe-garching.mpg.de/cdms). We thank the Cluster FGM team for their data. The EFW L3 data were obtained through the Cluster Active Archive (http://caa.estec.esa.int/caa). ACE spacecraft data were obtained through the CDAWeb (http://cdaweb.gsfc.nasa.gov).

References

Angelopoulos, V., Temerin, M., Roth, I., Mozer, F.S., Weimer, D., Hairston, M.R., 2002. Testing global storm-time electric field models using particle spectra on multiple spacecraft. Journal of Geophysical Research 107 (A8), 1194.

Baumjohann, W., Haerendel, G., 1985. Magnetospheric convection observed between 0600 and 2100 LT: solar wind and IMF dependence. Journal of Geophysical Research 90 (A7), 6370–6378.

Boonsiriseth, A., Thorne, R.M., Lu, G., Jordanova, V.K., Thomsen, M.F., Ober, D.M., Ridley, A.J., 2001. A semi-empirical equatorial mapping of AMIE convection electric potentials (MACEP) for the January 10, 1997, magnetic storm. Journal of Geophysical Research 106 (A7), 12903–12917.

Burton, R.K., McPherron, R.L., Russell, C.T., 1975. Journal of Geophysical Research 80, 4204–4214.

Carpenter, D.L., Giles, B.L., Chappell, C.R., Décréau, P.M.E., Anderson, R.R., Persoon, A.M., Smith, A.J., Corcuff, Y., Canu, P., 1993. Plasmasphere dynamics in the duskside bulge region: a new look at old topic. Journal of Geophysical Research 98, 19243–19271.

Darrouzet, F., et al., 2004. Density structures inside the plasmasphere: Cluster observations. Annales Geophysicae 19, 2577–2585.

Engwall, E., Eriksson, A.I., Andr, M., Dandouras, I., Paschmann, G., Quinn, J., Torkar, K., 2006. Low-energy (order 10 eV) ion flow in the mangetotail lobes inferred from spacecraft wake observations. Geophysical Research Letters 33, L06110.

Eriksson, A.I., Andr, M., Klecker, B., Laakso, H., Lindqvist, P.-A., Mozer, F., Paschmann, G., Pedersen, A., Quinn, J., Torbert, R., Torkar, K., Vaith, H., 2006. Electric field measurements on cluster: comparing the double-probe and electron drift techniques. Annales Geophysicae 24, 275–289.

Foster, J.C., Burke, W.J., 2002. SAPS: a new categorization for sub-auroral electric fields. Eos Transactions American Geophysical Union 83 (36), 393.

Friedel, R.H.W., Korth, H., Henderson, M.G., Thomsen, M.F., Scudder, J.D., 2001. Plasma sheet access to the inner magnetosphere. Journal of Geophysical Research 106 (A4), 5845–5858.

Galperin, Y., Ponomarev, Y., Zosimova, A., 1974. Plasma convection in the polar ionosphere. Annales de Geophysique 30, 1.

Garner, T.W., 2003. Numerical experiments on the inner magnetospheric electric field. Journal of Geophysical Research 108 (A10), 1373.

Goldstein, J., Sandel, B.R., Hairston, M.R., Reiff, P.H., 2003. Control of plasmaspheric dynamics by both convection and sub-auroral polarization stream. Geophysical Research Letters 30 (24), 2243.

Goldstein, J., Burch, J.L., Sandel, B.R., 2005. Magnetospheric model of subauroral polarization stream. Journal of Geophysical Research 110, A09222.

Gonzalez, W.D., Joselyn, J.A., Kamide, Y., Kroehl, H.W., Rostoker, G., Tsurutani, B.T., Vasyliunas, V.M., 1994. What is a geomagnetic storm? Journal of Geophysical Research 99 (A4), 5771–5792.

Gonzalez, W.D., Clua de Gonzalez, A.L., DalLago, A., Tsurutani, B.T., Arballo, J.K., Lakhina, G.K., Buti, B., Ho, C.M., Wu, S.-T., 1998. Magnetic cloud field intensities and solar wind velocities. Geophysical Research Letters 25, 963–966.

Gustafsson, G., et al., 2001. First results of electric field and density observations by Cluster EFW based on initial months of operation. Annales Geophysicae 19, 1219–1240.

Haaland, S.E., Paschmann, G., Foerster, M., Quinn, J.M., Torbert, R.B., McIlwain, C.E., Vaith, H., Puhl-Quinn, P.A., Kletzing, C.A., 2007. High-latitude plasma convection from Cluster EDI measurements: method and IMF-dependence. Annales de Geophysique 25, 239–253.

Huang, C.S., Sazykin, S., Spiro, R., Goldstein, J., Crowley, G., Ruohoniemi, J., 2006. Storm-time penetration electric fields and their effects. EOS Transactions American Geophysical Union 87 (13), 131.

Jordanova, V.K., Boonsiriseth, A., Thorne, R.M., Dotan, Y., 2003. Ring current asymmetry from global simulations using a high-resolution electric field model. Journal of Geophysical Research 108 (A12), 1443.

Jordanova, V.K., Miyoshi, Y.S., Zaharia, S., Thomsen, M.F., Reeves, G.D., Evans, D.S., Mouikis, C.G., Fennell, J.F., 2006. Kinetic simulations of ring current evolution during the Geospace Environment Modeling challenge events. Journal of Geophysical Research 111, A11S10.

Kamide, Y., et al., 1998. Current understanding of magnetic storms: storm–substorm relationships. Journal of Geophysical Research 103 (A8), 17705–17728.

Korth, H., Thomsen, M.F., Borovsky, J.E., McComas, D.J., 1999. Plasma sheet access to geosynchronous orbit. Journal of Geophysical Research 104 (A11), 25047–25061.

Liemohn, M.W., Kozyra, J.U., Thomsen, M.F., Roeder, J.L., Lu, G., Borovsky, J.E., Cayton, T.E., 2001. Dominant role of the asymmetric ring current in producing the stormtime *Dst**. Journal of Geophysical Research 106 (A6), 10883–10904.

Liemohn, M.W., Ridley, A.J., Gallagher, D.L., Ober, D.M., Kozyra, J.U., 2004. Dependence of plasmaspheric morphology on the electric field description during the recovery phase of the 17 April 2002 magnetic storm. Journal of Geophysical Research 109, A03209.

Liemohn, M.W., Ridley, A.J., Kozyra, J.U., Gallagher, D.L., Thomsen, M.F., Henderson, M.G., Denton, M.H., Brandt, P.C., Goldstein, J., 2006. Analyzing electric field morphology through data-model comparisons of the Geospace environment modeling inner magnetosphere/storm assessment challenge events. Journal of Geophysical Research 111, A11S11.

Lindqvist, P.-A., Khotyaintsev, Y., André, M., Eriksson, A.I., 2006. EFW data in the Cluster active archive. In: Proceedings of the Cluster and Double Star Symposium, 5th Anniversary of Cluster in Space, ESA SP-598.

Matsui, H., Quinn, J.M., Torbert, R.B., Jordanova, V.K., Baumjohann, W., Puhl-Quinn, P.A., Paschmann, G., 2003. Electric field measurements in the inner magnetosphere by Cluster EDI. Journal of Geophysical Research 108 (A9), 1352.

Matsui, H., Jordanova, V.K., Quinn, J.M., Torbert, R.B., Paschmann, G., 2004. Derivation of electric potential patterns in the inner magnetosphere from Cluster EDI data: initial results. Journal of Geophysical Research 109, A10202.

Maynard, N.C., Chen, A.J., 1975. Isolated cold plasma regions: observations and their relation to possible production mechanisms. Journal of Geophysical Research 80, 1009–1013.

Maynard, N.C., Aggson, T.L., Heppner, J.P., 1983. The plasmaspheric electric field as measured by ISEE 1. Journal of Geophysical Research 88, 3991–4003.

McComas, D.J., Bame, S.J., Baker, P., Feldman, W.C., Phillips, J.L., Riley, P., Griffee, J.W., 1998. Solar wind electron proton alpha monitor (SWEPAM) for the advanced composition explorer. Space Science Reviews 86, 563–612.

McIlwain, C.E., 1986. A K_p Dependent Equatorial Electric Field Model. Advances in Space Research 6 (3), 187–197.

Papitashvili, V.O., Rich, F., 2002. High-latitude ionospheric convection models derived from Defense Meteorological Satellite Program ion drift observations and parameterized by the interplanetary magnetic field strength and direction. Journal of Geophysical Research 107 (A8), 1198.

Papitashvili, V.O., Belov, B.A., Faermark, D.S., Feldstein, Ya.I., Golyshev, S.A., Gromova, L.I., Levitin, A.E., 1994. Electric potential patterns in the northern and southern polar regions parameterized by the interplanetary magnetic field. Journal of Geophysical Research 99 (A7), 13251–13262.

Paschmann, G., et al., 2001. The electron drift instrument on Cluster: overview of first results. Annales Geophysicae 19, 1273–1288.

Pedersen, A., Cattell, C.A., Falthammar, C.-G., Formisano, V., Lindqvist, P.-A., Mozer, F., Torbert, R., 1984. Quasistatic electric field measurements with spherical double probes on the GEOS and ISEE satellites. Space Science Reviews 37, 269–312.

Puhl-Quinn, P.A., Matsui, H., Mishin, E., Mouikis, C., Kistler, L., Khotyaintsev, Y., Décréau, P.M.E., Lucek, E., 2007. Cluster and DMSP observations of SAID electric fields. Journal of Geophysical Research, 112, A05219, doi:10.1029/2006JA012065.

Quinn, J.M., et al., 2001. Cluster EDI convection measurements across the high-latitude plasma sheet boundary at midnight. Annales Geophysicae 19, 1669–1681.

Richmond, A.D., Kamide, Y., 1988. Mapping electrodynamic features of the high-latitude ionosphere from localized observations: Technique. Journal of Geophysical Research 93 (A6), 5741–5759.

Ridley, A.J., Liemohn, M.W., 2002. A model-derived storm time asymmetric ring current driven electric field description. J. Geophysical Research 107 (A8), 1151.

Rowland, D.E., Wygant, J.R., 1998. Dependence of the large-scale, inner magnetospheric electric field on geomagnetic activity. Journal of Geophysical Research 103, 14959–14964.

Smith, C.W., L'Heureux, J., Ness, N.F., Acuña, M.H., Burlaga, L.F., Scheifele, J., 1998. The ACE magnetic fields experiment. Space Science Reviews 86, 613–632.

Spiro, R., Heelis, Hanson, W., 1979. Rapid subauroral ion drifts observed by Atmospheric Explorer C. Geophysical Research Letters, 6, 657.

Stern, D.P., 1975. The motion of a proton in the equatorial magnetosphere. Journal of Geophysical Research 80, 595.

Tsyganenko, N.A., 2002. A model of the near magnetosphere with a dawn–dusk asymmetry 1. Mathematical structure. Journal of Geophysical Research 107 (A8), 1179.

Vasyliunas, V.M., 1970. Mathematical models of magnetospheric convection and its coupling to the ionosphere. In: McCormac, B.M. (Ed.), Particles and Fields in the Magnetosphere. Reidel, Norwell, MA, p. 60.

Volland, H., 1973. A semiempirical model of large-scale magnetospheric electric fields. Journal of Geophysical Research 78, 171.

Weimer, D.R., 1996. A flexible, IMF dependent model of high-latitude electric potentials having "space weather" applications. Journal of Geophysical Research 23 (18), 2549–2552.

Weimer, D.R., 2001. An improved model of ionospheric electric potentials including substorm perturbations and application to the Geospace Environment Modeling November 24, 1996, event. Journal of Geophysical Research 106, 407–416.

Wolf, R.A., 1970. Effects of ionospheric conductivity on convective flow of plasma in the magnetosphere. Journal of Geophysical Research 75, 4677–4698.

Wygant, J., Rowland, D., Singer, H.J., Temerin, M., Mozer, F., Hudson, M.K., 1998. Experimental evidence on the role of the large spatial scale electric field in creating the ring current. J. Geophysical Research 103 (A12), 29527–29544.